

Study of the effect of morphological structure on microfiltration membrane fouling

Ming Zhuo^a, Kai Lv^a, Xueyan Zhang^a, Ying Zhang^a, Xizhi Shi^b, Yin Lu^{a,*}

^aCollege of Food and Pharmaceutical Sciences, Ningbo University, Qixingnan Road. 169, Ningbo, 315800, China, Tel. +86 13857400996; emails: luyin@nbu.edu.cn (Y. Lu), zhuoming92@163.com (M. Zhuo), 515748336@qq.com (K. Lv), 1581814358@qq.com (X. Zhang), 781092373@qq.com (Y. Zhang)

^bSchool of Marine Sciences, Ningbo University, Qixingnan Road. 169, Ningbo, 315800, China, email: shixizhi@nbu.edu.cn

Received 13 July 2018; Accepted 24 January 2019

ABSTRACT

Polysulfone and polyethersulfone membranes with sponge-like and finger-like structures were used to filter bovine serum albumin (BSA) solution at a constant flow rate. The relationship between the adsorption–retention cumulant of BSA and the transmembrane pressure (TMP) during the filtration process was analyzed. The experimental results show that the specific resistance of the filter cake is related to the pressure on the per-unit-thickness pressure-bearing layer (PPTPBL) of the membrane. The PPTPBL of the membrane with finger-like structures is large, which resulted in a high-resistance filter cake and led to the resistance of the filter cake increasing rapidly in the first filtration stage. The filter-cake layer broke under the effect of the rapidly increasing TMP and entered into the membrane to form difficult-to-clean fouling. The repeated breaking and formation of the cake layer makes the TMP fluctuate violently and rise slowly in the subsequent filtration process. However, the PPTPBL of the sponge-like-structure membrane is small; which resulted in a low-resistance and easy-to-clean filter cake forming on the surface during filtration.

Keywords: Membrane fouling; Membrane structure; Specific resistance; Transmembrane pressure; Pressure-bearing layer

1. Introduction

Microfiltration and ultrafiltration are commonly employed in the pharmaceutical, chemical, environmental, food, and dairy industries [1–4]. Membrane fouling restricts the further application of membrane separation technology. Membrane fouling is a process where a foulant is deposited on a membrane surface or into membrane pores, resulting in an increase in the filtration resistance and poor filtration performance. Blocking laws categorize fouling into four different regimes of complete blocking, standard blocking, intermediate blocking and cake filtration, which are based on the relative sizes of the foulants and pores and the process of surface deposition or cake accumulation [5–12].

Studies have shown that several factors make a difference in membrane fouling. The filtration liquid property is one such important factor that influences membrane fouling [13–16]. Changes in operating conditions such as transmembrane pressure (TMP), crossflow rates, filtrate concentration, temperature, and pretreatment, will also lead to changes in membrane fouling regimes [17–22]. Experiments have also shown that hydrophobic membranes and hydrophilic membranes have completely different performances when filtering solutions [23–26].

Through experiments, we found that the membrane structure also strongly affects the fouling character and cleaning effect. However, few articles have focused on these effects. Ho and Zydney [27,28] found that the fouling of track-etch membranes with straight-through pores occurred

* Corresponding author.

by pore blockage caused by the deposition of large protein aggregates on the membrane surface. Membranes with interconnected pores fouled more slowly since the fluid could flow around the blocked pores through the interconnected pore structure. Fan et al. [24] and Kang et al. [29] found that a thread-like morphology can limit the adsorption area and diminish irreversible fouling. The pore morphology may also affect the fouling by influencing the hydrophobic adsorption and size exclusion.

Membranes with finger-like and sponge-like pore structures are commonly used in engineering fields. However, the understanding of the morphological structure's effect on the membrane fouling is still limited. In this paper, we use bovine serum albumin (BSA) as the fouling component. Hydrophilic polysulfone (PSF) and polyethersulfone (PES) microfiltration membranes with finger-like and sponge-like pore structures and the same pore size were used to filter BSA solution at a constant flow rate. The TMP and BSA concentration of the filtrate were monitored in real time during the filtration process and the phenomenon of fouling and the fouling mechanisms were analyzed based on measured data. The relevant blocking laws were used to analyze the influence of the membrane structure on the membrane fouling mechanism.

2. Materials and methods

2.1. Materials

Hydrophilic polysulfone membranes with finger-like pore structures (PSF-F) (pore size $0.31\ \mu\text{m}$) and sponge-like pore structures (PSF-S) (pore size $0.30\ \mu\text{m}$) and hydrophilic PES membranes with finger-like pore structures (PES-F) (pore size $0.30\ \mu\text{m}$) and sponge-like pore structures (PES-S; pore size $0.29\ \mu\text{m}$) were used in this experiment. They were manufactured by a nonsolvent-induced phase separation method, and their water contact angle reduced to 0° within 1 min. Cross-sectional electron microscopy photomicrographs of the four membranes are shown as a2, b2, c2, and d2, respectively, in Fig. 4. BSA, MW 68,000, was acquired from Solarbio Science & Technology Co., Ltd. (Beijing).

A membrane pore size distribution apparatus based on the bubble point method and a membrane filter device were fabricated in our lab. The effective membrane filtration area was $1.13\ \text{cm}^2$. Scanning electron microscopy (SEM) was carried out on an FEI SIRION 200 from Hitachi, Ltd. (Japan). The

UV-Vis spectrophotometer was a L600-PDM from Beijing Purkinje General Instrument Co., Ltd. (China). The PPS-100 metering pump was purchased from Hangzhou Pupu Science Technology Co., Ltd. (China). The TMP was measured in real time using a Honeywell 4040PC pressure sensor.

2.2. Methods

The pore size distributions of the PSF and PES microfiltration membranes were measured using the pore size distribution apparatus based on the bubble point method. The membranes were soaked in isopropanol, and SEM was conducted to observe the morphological structure of the surface and cross sections of the PSF and PES microfiltration membranes. Specimens of representative membranes were cut out, their cross-sections were fractured after freezing with liquid nitrogen, and the surfaces were adhered to the sample stage with a conductive adhesive. The samples were placed in the electron microscope after they were plated with platinum under vacuum.

The BSA solution with a mass concentration of $1\ \text{mg mL}^{-1}$ was prepared and diluted to prepare solutions with different concentrations. The absorbance of these BSA solutions was measured at a wavelength of 278 nm. The standard curve equation was established as $A = 660.22 C$ according to the experimental data of the absorbance (A) and the mass concentration (C). The correlation coefficient R^2 was 0.999, demonstrating a good linear relationship between the absorbance and the mass concentration in the BSA concentration range from 0 to $1\ \text{mg mL}^{-1}$.

The experimental filter device is shown in Fig. 1. A triple valve was used to switch between line I, where the feed flowed directly to the UV-Vis spectrophotometer without passing through the membrane filter, and line II, where the feed passed through the membrane filter and the filtrate flowed to the UV-Vis spectrophotometer. A buffer tanker of volume 250 mL was used as a shock absorber to reduce the pressure fluctuations of the metering pump from ± 2 to $\pm 0.25\ \text{kPa}$. At the beginning of the experiment, the membrane was filtered with deionized water at a constant flow rate of $1\ \text{mL min}^{-1}$, and a pressure sensor was used to simultaneously detect the TMP (P_0). The BSA solution was pumped to the UV-Vis spectrophotometer directly through line I, and then the triple valve was rotated to allow the BSA solution to pump through line II for dead-end filtration. The absorbance

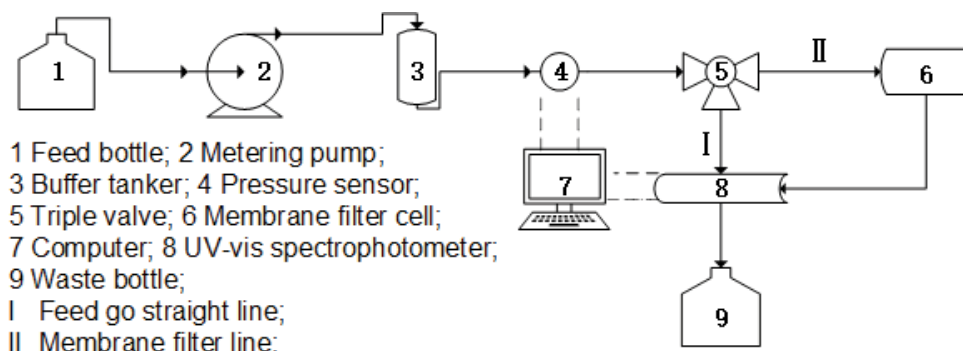


Fig. 1 Schematic diagram of the experimental filter device.

of the feed and filtrate over time was measured with the UV–Vis spectrophotometer in real time. The metering pump was maintained at a constant flow rate of 1 mL min⁻¹, and the ambient temperature was 25°C. The pressure sensor was used to measure the pressure change on the upstream side of the membrane in real time.

The adsorption–retention cumulant of the membrane for BSA was calculated according to Eq. (1):

$$Q = \frac{\sum \left\{ \left[(C_0 - C_{t(n)}) + (C_0 - C_{t(n+1)}) \right] / 2 \times [t_{(n+1)} - t_{(n)}] \right\} \times q \times 1,000}{S}, \quad (n = 1, 2, 3, 4, \dots) \quad (1)$$

where Q is the adsorption–retention cumulant on the membrane surface at time $t_{(n)}$ ($\mu\text{g cm}^{-2}$), C_0 is the initial concentration of the BSA feed solution (mg mL^{-1}), $t_{(n)}$ is the time at n (s), $C_{t(n)}$ is the concentration of the filtrate at time $t_{(n)}$ (mg mL^{-1}), q is the flow rate of the solution during filtration (mL s^{-1}), and S is the effective membrane filtration area (cm^2).

3. Results and discussion

Fig. 2 shows the variations of the absorbance and TMP of the four membranes of PSF and PES with finger-like and sponge-like pore structures during the filtration of the BSA solution. The BSA solution was passed through line I from 0 to 5 min. At this point, the triple valve was turned to direct the BSA solution through line II. When the filtrate started to pass

through line II, the absorbance value of the solution trended significantly upward. This behavior is attributed to the washing out of the soluble material in the membrane, which led to an increase in the absorbance. The corresponding data were ignored during the data processing.

Fig. 2 further shows that the absorbance of the filtrate tended to decrease with respect to the feed during the filtration process of the four membranes. This trend demonstrates that the four membranes had a certain adsorption–retention effect on the BSA. The retained BSA caused membrane fouling and led to an increase in the TMP. Eq. (1) was used to calculate the adsorption–retention cumulant Q during the filtration process. The correlation between Q and TMP over time is shown in Fig. 3.

Figs. 2 and 3 show that the TMP increased linearly with the filtration time during the filtration process of the PSF-S membrane and the PES-S membrane with sponge-like pore structures. By contrast, during the filtration process of the PSF-F membrane and the PES-F membrane with finger-like pore structures, the TMP varied in two stages. The TMP of the PSF-F membrane and the PES-F membrane showed a rapid linear increase in the first filtration stage (Fig. 3). In the second filtration stage, the TMP of the PSF-F membrane showed a severe fluctuation within a certain range during filtration. The TMP of the PES-F membrane also appeared to severely fluctuate but slowly increased.

Several different mechanisms for membrane fouling have been proposed: complete blocking, standard blocking, intermediate blocking, and cake filtration, as shown in Table 1 [6].

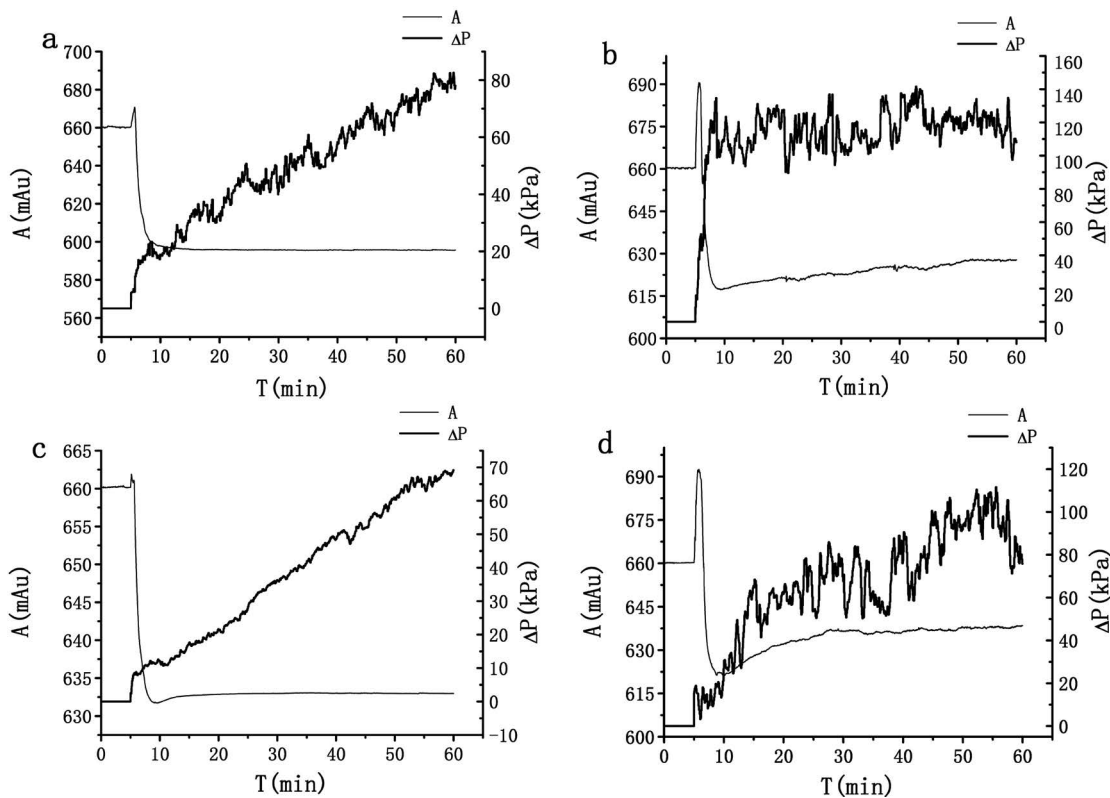


Fig. 2. Variation of absorbance and TMP when the BSA solution was filtered with four membranes, a: PSF-S, b: PSF-F, c: PES-S, d: PES-F.

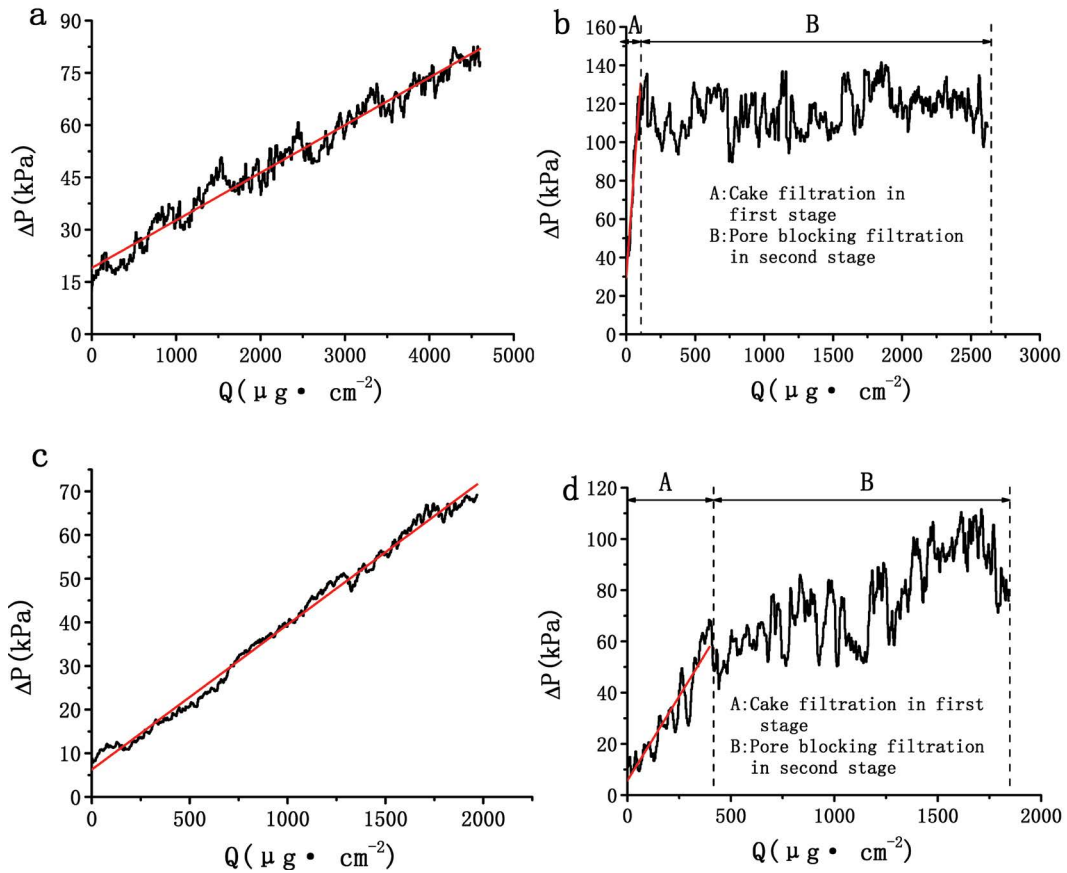


Fig.3. Variation of TMP of four membranes with Q , a: PSF-S, b: PSF-F, c: PES-S, d: PES-F.

The equations in Table 1 show that the TMP increases linearly with the filtrate volume only in the cake filtration model. Fig. 3 reveals that the TMP increased linearly with Q in the filtration process of the PSF-S membrane and the PES-S membrane and in the first filtration stage of the PSF-F membrane (the range of Q was 0–104 $\mu\text{g cm}^{-2}$) and the first filtration stage of the PES-F membrane (the range of Q was 0–397 $\mu\text{g cm}^{-2}$). The TMP of the PSF-F membrane fluctuated drastically in the second filtration stage within the range from 93 to 140 kPa and no longer increased and the TMP of the PES-F membrane in the second filtration stage also fluctuated but continued to slowly increase. The entire filtration process of the PSF-S membrane and the PES-S membrane as well as the first filtration stages of the PSF-F membrane and the PES-F membrane all show typical cake filtration characteristics.

In Table 1, the cake filtration model is given by Eq. (2):

$$\Delta P = \Delta P_0 + \frac{q\mu a^* c_b}{S^2} \times V \quad (2)$$

The adsorption–retention cumulant of BSA ($Q = C_b \times V$) can be directly calculated from Eq. (1) according experimental data. Thus, Eq. (2) can be simplified to Eq. (3):

$$\Delta P = \Delta P_0 + K^* Q \quad (3)$$

where

$$K^* = \frac{q\mu}{S^2} a^* \quad (4)$$

The experimentally measured ΔP and the calculated Q are correlated according to Eq. (3) for the entire filtration stage of the PSF-S membrane and the PES-S membrane with sponge-like pore structures and for the initial filtration stages of PSF-F membrane and PES-F membrane with finger-like pore structures. During the experiment, $q = 1/60 \text{ mL s}^{-1}$, $\mu = 0.8949 \times 10^{-3} \text{ Pa s}$, and $S = 1.13 \text{ cm}^2$. a^* was directly calculated according to the fitting result of K^* , and the results are shown in Table 2.

The values in Table 2 reveal that the a^* for the cakes on the PSF-S membrane and the PES-S membrane with sponge-like pore structures were smaller, whereas those for the cakes on the PSF-F membrane and the PES-F membrane with finger-like pore structures were larger. These results show that the a^* of the filter cake differs for membranes composed of the same material but with different structures. However, the values of a^* were roughly equivalent for the membranes composed of different materials but with the same structure. Thus, the specific resistance of the filter cake is related to the membrane structure.

SEM micrographs of the used membranes are shown in Fig. 4. The morphological structures of the PSF-S membrane

Table 1
Summary of constant flux blocking laws [6]

Model	Integrated equation	First derivative
Complete blocking	$\Delta P = \frac{q\mu R}{S - \sigma V} = \frac{\Delta P_0}{1 - (\sigma/S)V}$	$\frac{d\Delta P}{dV} = \frac{\sigma \Delta P_0 / S}{1 - [1 - (\sigma/S)V]^2}$
Standard blocking	$\Delta P = \frac{\Delta P_0}{(1 - K_s V / 2)^2}$	$\frac{d\Delta P}{dV} = \frac{\Delta P_0 K_s}{(1 - K_s V / 2)^3}$
Intermediate blocking	$\Delta P = \Delta P_0 \exp\left(\frac{\sigma}{S} V\right)$	$\frac{d\Delta P}{dV} = \frac{\Delta P_0 \sigma}{S} \exp\left(\frac{\sigma}{S} V\right)$
Cake filtration	$\Delta P = \Delta P_0 + \frac{q\mu a^* c_b}{S^2} V$	$\frac{d\Delta P}{dV} = \frac{q\mu a^* c_b}{S^2}$

P is the TMP, P_0 is the initial TMP, q is the filtration rate, R is the clean membrane resistance, C_b is the amount of material deposited on (or within) the membrane per unit filtrate volume, V is the cumulative volume filtered, μ is the absolute viscosity, σ is the clogging coefficient, a^* is the specific cake resistance on a mass basis, $a^* = \beta \Delta P^{n_1}$ where β and n_1 are compressibility parameters, $K_s = \frac{2C}{\pi L N r_0^2} = \frac{2C}{L \varepsilon S^2}$, and $K_c = \frac{q\mu c_b a_0^*}{S^2}$.

Table 2
Correlated results according to Eq. (3) and the related parameters

	$\Delta P = \Delta P_0 + k'Q$	R^2	K' (kPa cm ² μg ⁻¹)	$a^* \times 10^{-12}$ (m kg ⁻¹)
PSF-S	$\Delta P = 19.01149 + 0.01366Q$	0.96911	0.01366	19
PSF-F	$\Delta P = 27.8125 + 1.05518Q$	0.94032	1.05518	1,507
PES-S	$\Delta P = 6.26323 + 0.0332Q$	0.99307	0.0332	47
PES-F	$\Delta P = 5.71149 + 0.13138Q$	0.86424	0.13138	187

and the PES-S membrane still contained uniform sponge-like pore structures, but the membrane structures of the PSF-F and PES-F membranes contained a dense surface layer together with the finger-like macropores.

The fluid flow in membrane pores can be characterized by Hagen-Poiseuille’s law:

$$J = \frac{\varepsilon r^2}{8\mu\tau} \times \frac{\Delta P}{L_m} \tag{5}$$

and

$$\varepsilon = \frac{n_p \pi r^2}{S} \tag{6}$$

where J is the fluid flux, r is the pore size, ΔP is the TMP over membrane thickness L_m , τ is the pore tortuosity, ε is the surface void rate, and n_p is the through-hole number. The relationship between ΔP and r can be expressed as:

$$\Delta P = \frac{8J\mu\tau L_m}{n_p \pi r^4} \tag{7}$$

The ΔP at a constant flux is inversely proportional to r^4 in Eq. (7). The membrane structure is evenly distributed

and the pore size of the membranes with sponge-like pore structures is approximately the same. Thus, the TMP over the membrane thickness was evenly distributed. The thickness of the pressure-bearing layer could be considered the thickness of the membrane (see a2, c2 in Fig. 4). The pore size in the finger-like macropores was much larger than that in the surface layer for the membrane with finger-like pore structures. Therefore, the pressure drop produced in the finger-like macropores was much smaller than that in the surface pores and can be ignored. We considered the surface layer to be the pressure-bearing layer.

We measured the initial TMP (P_0) of the clean membrane filtering deionized water. The thickness of the pressure-bearing surface layer (L) of the membrane with finger-like pore structures was measured from the surface of the membrane to the position where the pore size changes drastically according to the SEM photograph (see b2 and d2 in Fig. 4). The pressure on the per-unit-thickness pressure-bearing layer (PPTPBL) was calculated and the result is shown in Table 3. We related the a^* of the filter cake to the PPTPBL (P_0/L) as shown in Fig. 3. The PPTPBL exhibited good correlation with a^* for the PSF-S, PSF-F, PES-S, and PES-F membranes. The PPTPBL and the a^* were large for the membranes with the finger-like pore structures and small for the membranes with the sponge-like pore structures. The PPTPBL strongly influenced the a^* of the filter cake. We correlated the a^* of the

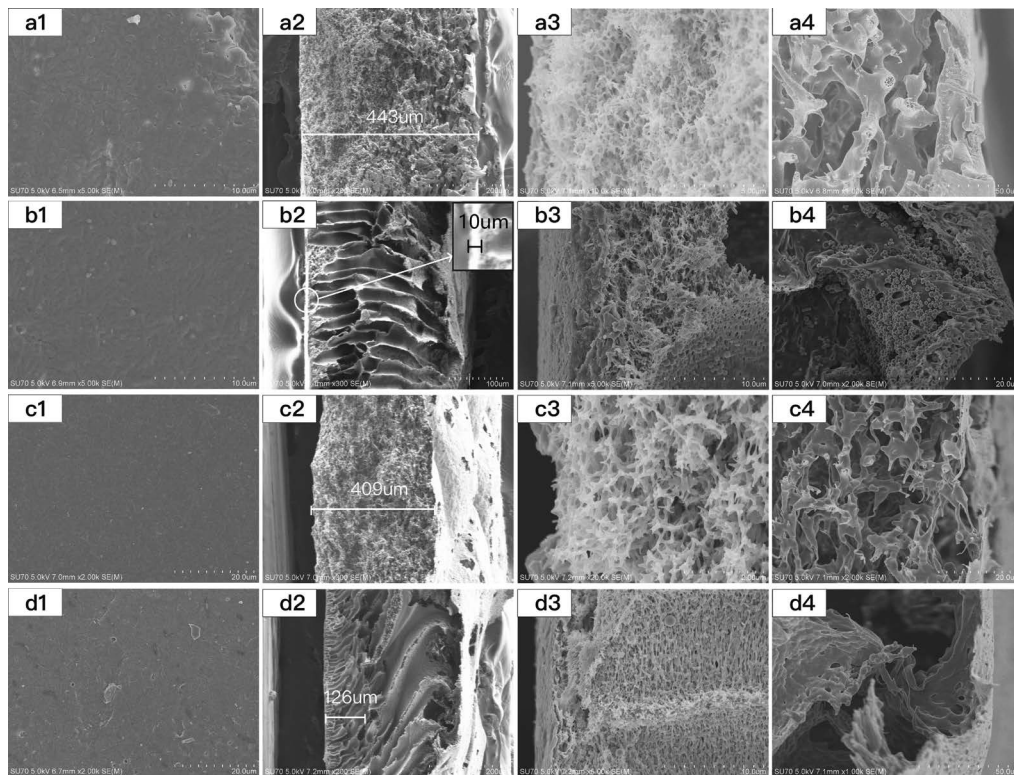


Fig. 4. SEM micrographs of the four membranes after filtration, a: PSF-S, b: PSF-F, c: PES-S, d: PES-F, where 1 is the upper surface, 2 is the cross section, 3 is the upper cross section, and 4 is the lower cross section.

Table 3
PPTPBL and a^* for four types of membranes

	P_0 (kPa)	L (μm)	P_0/L (kPa μm^{-1})	$a^* \times 10^{-12}$ (m kg^{-1})
PSF-S	14	433	0.0316	19
PSF-F	16	10	1.6	1,507
PES-S	16	409	0.0342	47
PES-F	20	126	0.158	187

filter cake according to the compressible cake model [30].

The correlation result was $a^* = 1020.89 \frac{P_0^{0.859}}{L} - 21.08$, where the correlation coefficient R^2 was 0.99943, see Fig. 5. It could be seen that the a^* of the filter cake was related to the PPTPBL with a compressibility factor of 0.859 when the BSA solution was filtered through membranes with different structures.

The specific resistance of the filter cake represents the filtration resistance caused by a unit mass of the adsorption–retention cumulant per unit membrane area. The PPTPBL represents the pressure drop generated from a unit thickness of the pressure-bearing layer of the membrane. The PPTPBL could be reasonably deemed to characterize the pressure exerted on the surface layer of the membrane. The experiment found that the PPTPBL has a close relationship with the specific resistance of the filter cake. This is because BSA is a macromolecular substance. The accumulation form of BSA that is initially deposited on the membrane surface layer changes under different pressures. BSA forms a thinner and denser filter cake under higher pressure, resulting in a higher specific resistance, while a looser cake is formed and the

specific resistance is lower under a lower pressure. Thus, the BSA filter cake layer shows compressibility.

In the filtration process for membranes with sponge-like pore structures, the PPTPBL was small because the TMP was evenly distributed over the entire membrane. The small PPTPBL leads to a loose filter cake and a small a^* . However, the PPTPBL was large due to the uneven pressure distribution in the membrane with finger-like structures. The resulting filter-cake layer was dense and a^* was large. A small amount of adsorption–retention cumulant would thus cause a rapid increase in the TMP. The dense and thin layer of the filter cake formed quickly as the filtration progressed. The extremely high pressure on the ultrathin cake layer led to the cake on the surface pores of the membrane breaking and being pushed into the membrane. A new cake layer was rapidly formed on the membrane surface in the subsequent filtration process. The phenomenon of the cake layer repeatedly forming and breaking caused the TMP on the membrane with finger-like pore structures to fluctuate in the second filtration stage. The contaminants that are pushed into the macropores are further taken out from the bottom layer of the membrane, thereby causing an increase in the filtrate concentration of BSA in the membranes with finger-like pore structures. This phenomenon was observed in the experiment as shown in 'b' and 'd' in Fig. 2, where the absorbance of the filtrate increased in the second filtration stages of the PES-F and PSF-F.

As shown in Fig. 4, cake layers were observed on the top surfaces of the four membranes. The SEM micrographs of the cross sections of the PSF-S membrane and the PES-S

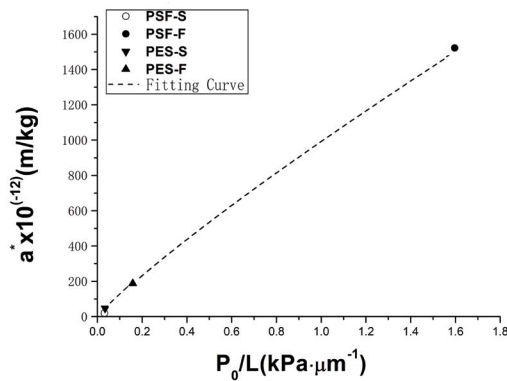


Fig. 5. Relationship between the membrane structure and the specific resistance of the filter cake.

membrane show no residual fouling inside the membrane pores. However, residual fouling remained inside the finger-like pores of the PSF-F membrane and the PES-F membrane, with the residual fouling in the PSF-F membrane being more serious. We reasonably speculated that the residual fouling in the membrane with the sponge-like structure generated a low-specific-resistance loose filter cake on the membrane surface. The increased TMP was evenly distributed on the filter cake, and the pressure drop on the surface of the membrane was not large. Therefore, the foulant was not pressed into the membrane pores.

The surface pressure-bearing layer of the PSF-F membrane was thinner than that of the PES-F membrane (Fig. 4). The PPTPBL of the PSF-F membrane was therefore greater, which resulted in a denser cake layer with a larger a . The increase in the TMP was faster with Q in the first filtration stage. The ultrathin layer of cake was more likely to break and be pushed into the finger-like pores of the PSF-F membrane. The residual fouling in the PSF-F membrane was more serious than that in the PES-F membrane. In contrast, only part of the cake on the membrane surface pores was broken in the PES-F membrane. This part of the foulant was pressed into the membrane pores, but the unbroken part of the cake layer continued to accumulate, and the TMP of the PES-F membrane fluctuated substantially but still slowly increased.

The residual fouling inside the membranes made the membranes difficult to clean. To demonstrate this effect, we cleaned the used membranes with flowing deionized water and measured the water fluxes again. The flux recovery rate was calculated by comparison with the initial fluxes of the clean membranes, and the results are shown in Table 4. The flux recovery rates of the PSF-S membrane and PES-S membrane with sponge-like pore structures were 88% and 93%, respectively, whereas the flux recovery rates of the PSF-F membrane and PES-F membrane with finger-like pore structures were 33% and 45%, respectively. The membranes with sponge-like pore structures were easier to clean than the membranes with finger-like pore structures. Furthermore, the PSF-F membrane was harder to clean than the PES-F membrane. These results confirm previous assumptions that the fouling of the membranes with sponge-like pore structures occurred only on the membrane surface and was easy to clean, whereas the fouling of the membranes with finger-like pore structures occurred both on the membrane

Table 4

Water fluxes of membranes and their recovery rates

	Initial water flux (L h ⁻¹ m ⁻²)	Water flux for cleaned membranes (L h ⁻¹ m ⁻²)	Water flux recovery rate (%)
PSF-S	2,484.07	2,197.45	88
PSF-F	2,866.24	955.41	33
PES-S	3,057.32	2,866.24	93
PES-F	2,292.99	1,050.95	45

surface and inside the membrane pores, making it difficult to clean.

4. Conclusions

The fouling performance of BSA solution on membranes with different structures was studied. The concept of the pressure-bearing surface layer is proposed. The PPTPBL is calculated to characterize the pressure exerted on the surface layer of a membrane. The entire filtration process of the membranes with sponge-like pore structures (PSF-S and PES-S membranes), as well as the first filtration stages of the membranes with finger-like pore structures (PSF-F and PES-F membranes) show typical cake filtration characteristics.

The experiment shows that the specific resistance of the filter cake in the initial filtration stage is positively related to the PPTPBL of the membrane. This caused differences in the membrane fouling model and cleaning performance between the membranes with finger-like and sponge-like morphological structures.

The structures of the membranes with sponge-like pore structures are uniform and the PPTPBL is small. This caused the formation of a loose filter cake and low specific resistance. The fouling cake remained on the membrane surface and thus could be easily cleaned. The TMP increases linearly with the adsorption–retention cumulant of fouling during filtration.

The membranes with finger-like structures contained finger-like macropores and dense surface layers. The TMP is distributed mainly on the dense surface layer, which results in a large PPTPBL and led to the formation of a dense cake layer of high specific resistance in the first filtration process. A small adsorption–retention cumulant of fouling resulted in a rapid increase in the TMP. The high pressure broke the cake layer on the membrane pores, and the foulant was pushed inside the membrane pores. A new cake layer rapidly formed on the membrane surface in the subsequent filtration process. The phenomenon of the cake layer repeatedly forming and breaking caused the TMP on the membranes with finger-like pore structures to fluctuate in the second filtration stage. The foulant that remained inside the membrane pores made the membrane cleaning more difficult.

Acknowledgements

The authors would like to acknowledge the sponsorship of the National Natural Science Foundation of China (Grant No. 31772856) and the K.C. Wong Magna Fund in Ningbo University.

Symbols

ΔP	—	Transmembrane pressure (TMP), kPa
Q	—	Adsorption–retention cumulant (ARC) on the membrane surface, $\mu\text{g cm}^{-2}$
C_0	—	Initial concentration of the BSA feed solution, mg mL^{-1}
$t^{(n)}$	—	Filtration time, s
$C^{(n)}$	—	Concentration of filtrate at time $t^{(n)}$, mg mL^{-1}
q	—	Flow rate of the solution during filtration, mL s^{-1}
S	—	Effective membrane filtration area, cm^2
C_b	—	Amount of material deposited on (or within) the membrane per unit filtrate volume, ug m^{-3}
V	—	Cumulative volume filtered, mL
μ	—	Absolute viscosity, Pa-s
σ	—	Clogging coefficient
n_1	—	Compressibility parameter
β	—	Compressibility parameter
$a^* \times 10^{-12}$	—	Specific cake resistance, m kg^{-1}
J	—	Fluid flux, m s^{-1}
τ	—	Pore tortuosity
r	—	Pore size, μm
ε	—	Surface void rate
n_p	—	Through-hole number
L_m	—	Membrane thickness, μm
L	—	Length of the thickness of the pressure-bearing surface layer, μm

References

- S.A. Snyder, S. Adham, A.M. Redding, F.S. Cannon, J. Decarolis, J. Oppenheimer, E.C. Wert, Y. Yoon, Role of membranes and activated carbon in the removal of endocrine disruptors and pharmaceuticals, *Desalination*, 202 (2007) 156–181.
- R.W. Baker, *Membrane Technology and Applications*, 2nd Ed., Wiley, Chichester, 2004.
- S. Judd, C. Judd, *The MBR Book: Principles and Applications of Membrane Bioreactors for Water and Wastewater Treatment*, 2nd Edn., Elsevier, Oxford, 2011.
- G. Daufin, J.P. Escudier, H. Carrere, S. Berot, L. Fillaudeau, M. Decloux, Recent and emerging applications of membrane processes in the food and dairy industry, *Food Bioprod. Process.*, 79 (2001) 89–102.
- M. Hlavacek, F. Bouchet, Constant flowrate blocking laws and an example of their application to dead-end microfiltration of protein solutions, *J. Membr. Sci.*, 82 (1993) 285–295.
- S. Chellam, W. Xu, Blocking laws analysis of dead-end constant flux microfiltration of compressible cakes, *J. Colloid Interface Sci.*, 301 (2006) 248–257.
- G. Bolton, L.C. Dan, R. Kuriyel, Combined models of membrane fouling: Development and application to microfiltration and ultrafiltration of biological fluids, *J. Membr. Sci.*, 277 (2006) 75–84.
- F. Wang, V.V. Tarabara, Pore blocking mechanisms during early stages of membrane fouling by colloids, *J. Colloid Interface Sci.*, 328 (2008) 464–469.
- A. Zarragoitia-González, S. Schetrite, M. Alliet, U. Jáuregui-Haza, C. Albasi, Modelling of submerged membrane bioreactor: Conceptual study about link between activated sludge biokinetics, aeration and fouling process, *J. Membr. Sci.*, 325 (2008) 612–624.
- S. Chellam, N.G. Cogan, Colloidal and bacterial fouling during constant flux microfiltration: comparison of classical blocking laws with a unified model combining pore blocking and EPS secretion, *J. Membr. Sci.*, 382 (2011) 148–157.
- D. Franco, A. Mato, F.J. Salgado, M. Lópezpedrouso, M. Carrera, S. Bravo, M. Parrado, J.M. Gallardo, C. Zapata, Tackling proteome changes in the longissimus thoracis bovine muscle in response to pre-slaughter stress, *J. Proteomics*, 122 (2015) 73–85.
- Y. Shen, W. Zhao, K. Xiao, X. Huang, A systematic insight into fouling propensity of soluble microbial products in membrane bioreactors based on hydrophobic interaction and size exclusion, *J. Membr. Sci.*, 346 (2010) 187–193.
- M. Ahsani, R. Yegani, Study on the fouling behavior of silica nanocomposite modified polypropylene membrane in purification of collagen protein, *Chem. Eng. Res. Des.*, 102 (2015) 261–273.
- M. Ahsani, M.D. Havigh, R. Yegani, Fouling mechanisms during protein microfiltration: the effects of protein structure and filtration pressure on polypropylene microporous membrane performance, *Polyolefins J.*, 4 (2017) 175–189.
- C. Rai, P. Rai, G.C. Majumdar, S. De, S. Dasgupta, Mechanism of permeate flux decline during microfiltration of watermelon (*Citrullus lanatus*) juice, *Food Bioprocess Technol.*, 3 (2010) 545–553.
- M.K. Purkait, P.K. Bhattacharya, S. De, Membrane filtration of leather plant effluent: flux decline mechanism, *J. Membr. Sci.*, 258 (2005) 85–96.
- M.C.V. Vela, S. Álvarez Blanco, J. Lora García, E. Bergantiños Rodríguez, Analysis of membrane pore blocking models adapted to crossflow ultrafiltration in the ultrafiltration of PEG, *Chem. Eng. J.*, 149 (2009) 232–241.
- S.J. Lee, M. Dilaver, P.K. Park, J.H. Kim, Comparative analysis of fouling characteristics of ceramic and polymeric microfiltration membranes using filtration models, *J. Membr. Sci.*, 432 (2013) 97–105.
- F. Lotfi, B. Samali, D. Hagare, Cleaning efficiency of the fouled forward osmosis membranes under different experimental conditions, *J. Environ. Chem. Eng.*, 6 (2018) 4555–4563.
- F. Arndt, F. Ehlen, S. Schütz, H. Anlauf, H. Nirschl, Influence of operating parameters and membrane materials on fouling of ceramic hollow fibre membranes, *Sep. Purif. Technol.*, 171 (2016) 289–296.
- Y. Luo, P. Ledech, R.K. Henderson, Assessment of membrane photobioreactor (MPBR) performance parameters and operating conditions, *Water Res.*, 138 (2018) 169–180.
- H. Cho, Y. Choi, S. Lee, Effect of pretreatment and operating conditions on the performance of membrane distillation for the treatment of shale gas wastewater, *Desalination*, 437 (2018) 195–209.
- I.S. Chang, S.O. Bag, C.H. Lee, Effects of membrane fouling on solute rejection during membrane filtration of activated sludge, *Process Biochem.*, 36 (2001) 855–860.
- H. Fan, K. Xiao, S. Mu, Y. Zhou, J. Ma, X. Wang, X. Huang, Impact of membrane pore morphology on multi-cycle fouling and cleaning of hydrophobic and hydrophilic membranes during MBR operation, *J. Membr. Sci.*, 556 (2018) 312–320.
- Z. Li, D. Rana, Z. Wang, T. Matsuura, C.Q. Lan, Synergic effects of hydrophilic and hydrophobic nanoparticles on performance of nanocomposite distillation membranes: an experimental and numerical study, *Sep. Purif. Technol.*, 202 (2018) 45–58.
- D.C. Banti, P. Samaras, C. Tsiptsias, A. Zouboulis, M. Mitrakas, Mechanism of SMP aggregation within the pores of hydrophilic and hydrophobic MBR membranes and aggregates detachment, *Sep. Purif. Technol.*, 202 (2018) 119–129.
- C.C. Ho, A.L. Zydney, Effect of membrane morphology on the initial rate of protein fouling during microfiltration, *J. Membr. Sci.*, 155 (1999) 261–275.
- C.C. Ho, A.L. Zydney, Theoretical analysis of the effect of membrane morphology on fouling during microfiltration, *Sep. Sci. Technol.*, 34 (1999) 2461–2483.
- X. Kang, J. Sun, Y. Mo, F. Zhou, L. Peng, H. Xia, J. Ma, B. Ma, Effect of membrane pore morphology on microfiltration organic fouling: PTFE/PVDF blend membranes compared with PVDF membranes, *Desalination*, 343 (2014) 217–225.
- F.M. Tiller, C.S. Yeh, Relative liquid removal in filtration and expression, *Filtr. Sep.*, 27 (1990) 129–135.

Supplementary Information

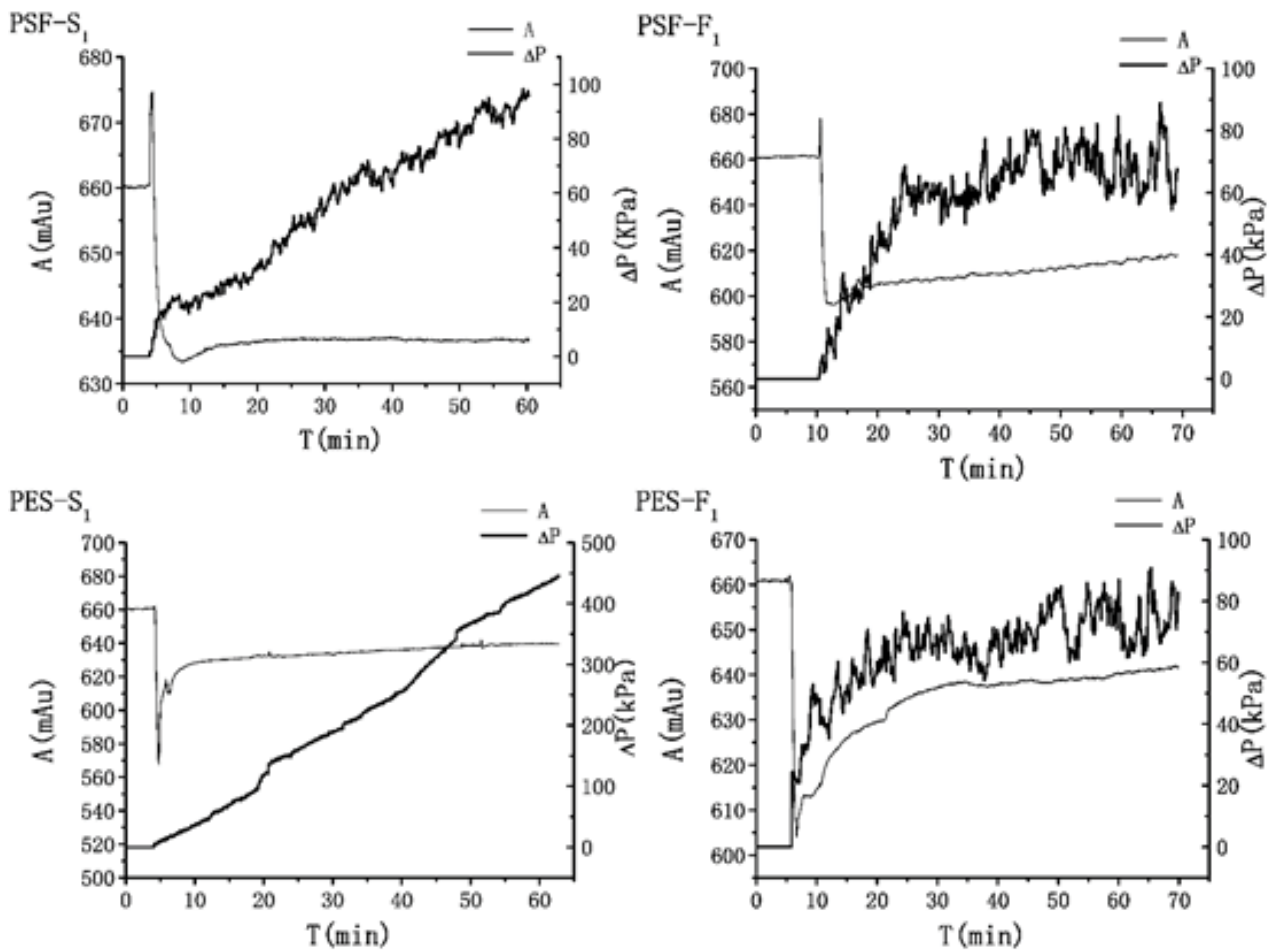


Fig. S1. Repeated experiments, variation of absorbance and TMP when the BSA solution was filtered with PSF-S₁, PSF-F₁, PES-S₁, PES-F₁ membranes.

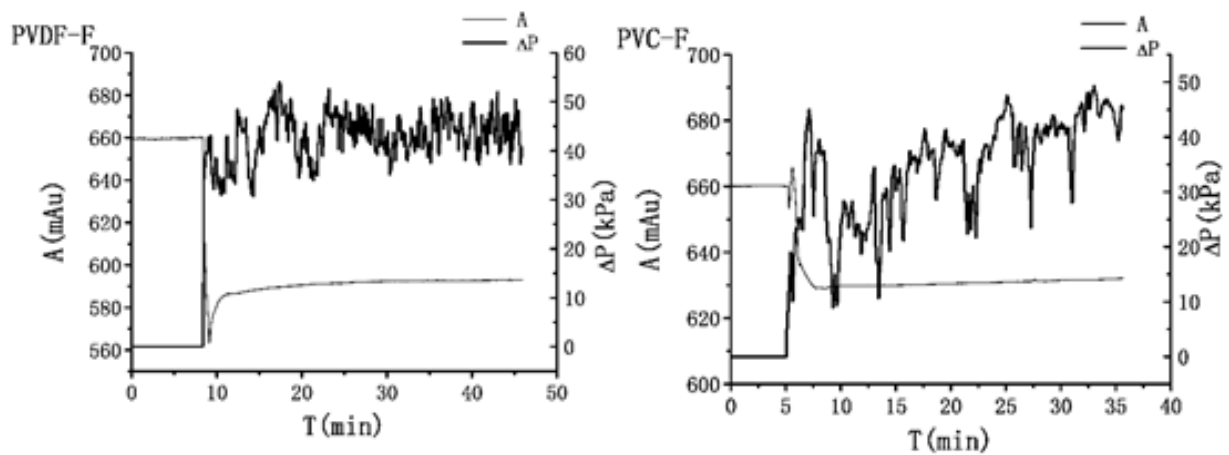


Fig. S2. Variation of absorbance and TMP when the BSA solution was filtered with PVDF membrane and PVC membrane with finger-like pore structure.

The repeated experiments of PES-F₁, PSF-F₁ membranes and PVC, PVDF membranes with finger-like pore structure and the repeated experiments of PES-S₁, PSF-S₁ membranes with sponge-like pore structure reveal the same law described in the paper, see Figs. S1 and S2. The water contact angle of polysulfone membrane and polyethersulfone membrane are shown in Fig. S3.

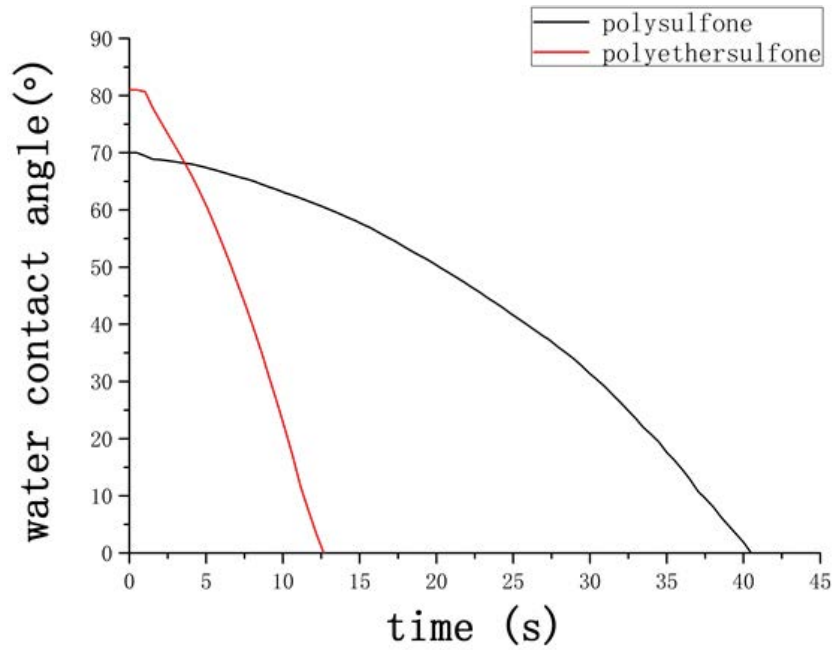


Fig. S3. Water contact angle of polysulfone membrane and polyethersulfone membrane.